Ionization-seeded current filamentation in expanding plasma sheaths

Audrey Farrell,[1,*] Mitchell Sinclair,[1] Yipeng Wu,[1,2] Kenneth A. Marsh,[1] Apurva Gaikwad,[3]
Navid Vafaei-Najafabadi,[3,4] Marcus Babzien,[4] William Li,[4] Mikhail Polyanskiy,[4] Igor Pogorelsky,[4]
Chaojie Zhang,[1] and Chandrashekhar Joshi[1]

[1]*Department of Electrical and Computer Engineering, University of California, Los Angeles, Los Angeles, California, USA*
[2]*School of Physics and Astronomy, Shanghai Jiao Tong University, Shanghai, China*
[3]*Department of Physics and Astronomy, Stony Brook University, Stony Brook, New York, USA*
[4]*Accelerator Test Facility, Brookhaven National Laboratory, Upton, New York, USA*

(Received 13 January 2026; accepted 21 July 2026; published 27 August 2026)

We report a seeding mechanism for the current filamentation instability that was identified using an experimental platform where a relativistically intense 2-ps (full width at half maximum) long-wavelength infrared pump laser both produces and interacts with a plasma that is overdense to the pump yet transparent to a near-infrared probe laser. This platform enables simultaneous high spatial resolution measurements of the self-generated magnetic filaments using Faraday rotation polarimetry and density filaments using interferometry. Supporting simulations show that the highly nonlinear dependence of the ionization rate on the local sheath electric field produced by pump-laser-heated hot electrons gives rise to 20-μm-scale filaments of cold electrons that form a return current, generating local azimuthal magnetic fields that can last for over 100 picoseconds.

DOI: 10.1103/gk4q-v1rm

I. INTRODUCTION

Transport of energetic electrons through dense plasma is a fundamental but complex process in high-energy-density physics, critical to applications such as fast-ignition-based inertial confinement fusion [1] and laser-driven ion acceleration [2]. This transport is often influenced by self-generated magnetic fields [3]. Mechanisms such as the Biermann-battery effect [4,5], also known as the $(\nabla n_e \times \nabla T_e)$ effect, Weibel instability [6], and current filamentation instability (CFI) [7], are known to amplify magnetic fields to megagauss (MG) levels in these plasmas. Together with space-charge effects [8–10] the magnetic fields can modulate and spread the fast electron beam and affect its energy transport and ultimate deposition.

While these mechanisms are ubiquitous in laboratory and astrophysical plasmas, their development in the overdense region of laser-produced plasmas remains under diagnosed. The high plasma densities $(10^{21} < n_e < 10^{24}\ \mathrm{cm}^{-3})$ and steep density gradients in solid-target plasmas render them opaque to optical probes. Consequently, our understanding of this regime relies heavily on simulations and indirect experimental inferences, such as images of electron-beam breakup after exiting the target [11], structures in images of optical emission due to transition and Čerenkov radiation [12], or absorption of probe light by solid-density plasma [13]. Recent advances in x-ray microscopy have allowed density modulations due to CFI to be observed in a solid target for the first time [14], but the magnetic field strength had to be inferred from models of density filament mergers. How these instabilities are seeded and evolve within the overdense plasma are key unanswered questions.

Extensive laboratory work has explored the above instabilities in more accessible regimes using lower-density gas targets. Thermal Weibel instability, driven by temperature anisotropy [6], has been measured in underdense optical-field-ionized plasmas with known electron velocity distributions [5,15–17], including in a transversely bounded plasma [18]. Other studies have characterized the filamentation of external relativistic electron beams propagating through a plasma [19–21] and the ion-driven Weibel instability in counter-streaming plasma flows [22,23]. To make it easier to access the overdense region, the wavelength of the pump laser can also be increased. Such overdense laser plasmas can remain transparent to optical probes. While this particular regime is overdense, it is not a perfect analog of laser-solid interactions, since the plasma is generally collisionless. Leveraging this collisionless regime in comparison to highly collisional solid-density experiments may allow us to gain insight into the role of collisions in these interactions.

In this paper, we report a seeding mechanism that generates megagauss-strength, filamentary magnetic fields that begins with electric-field hot spots in the expanding plasma sheath. Due to the nonlinear dependence of the ionization rate on the local electric field [24–26], these hot spots cause further ionization, generating density filaments of cold plasma [3,27] as the sheath field expands through partially ionized or neutral gas. This transverse instability of the ionization front has certain similarities to streamers observed in discharge plasmas [28,29], where an applied static electric field causes seed plasma to develop a branching ionization front. While streamers occur in highly collisional plasma with negligible magnetic fields, that is not the case in the collisionless

*Contact author: audfarrell@g.ucla.edu

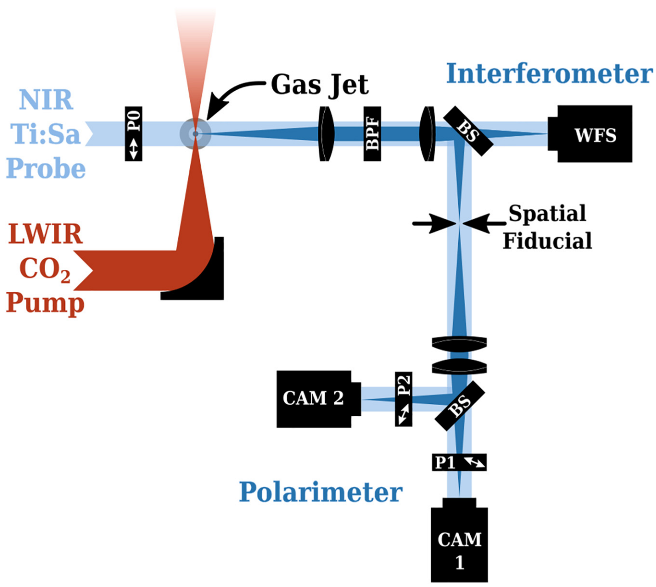

FIG. 1. Sketch of experimental setup. P0, P1, and P2 are linear polarizers, WFS is a wave-front sensor, and BPF is a bandpass filter centered at $\lambda^{\text{probe}} = 800$ nm.

plasma discussed here. Theoretical work modeling electron-beam filamentation in solid dielectrics has identified a related corrugation instability [30,31]. In the highly collisional regime, the ionization front velocity has a nonlinear dependence on the electron-beam density due to collisional ionization, and so deflection of beam electrons into regions of higher local beam density forms a positive-feedback loop for a filament to develop. In the lower density, collisionless regime studied here, the ionization front is driven by field ionization due to a surplus of ions at the ionization front as ionized cold electrons form the return current. These filaments of cold electrons forcibly seed CFI by counterstreaming against the expanding hot electrons, creating ∼20-μm-scale current filaments surrounded by MG magnetic fields that last for more than 100 ps, far longer than the pump-laser pulse duration.

II. EXPERIMENTAL SETUP

In this work (see Fig. 1) a relativistic intensity (normalized vector potential $a_0 = eA/m_ec > 1$), where A is the amplitude of the laser vector potential, 2.5-J short-pulse ($\tau_{\text{FWHM}} = 2$ ps) long-wavelength infrared (LWIR) ($\lambda = 9.2$ μm) CO_2 was used to produce an overdense plasma. The laser ionized a 2-mm-diameter plume of nitrogen gas multiple times to exceed the critical density $n_c = m_e\omega_0^2/4\pi e^2 = 1.3 \times 10^{19}$ cm^{-3} [defined as the density where the plasma frequency $\omega_p = (4\pi n_e e^2/m_e)^{1/2}$ is equal to the laser frequency ω_0]. The LWIR laser was linearly polarized and focused down to a 35-μm spot size, with typical a_0 between 1.5 and 2. The probe laser (an 80-fs near-infrared, $\lambda^{\text{probe}} = 800$ nm, $n_c^{\text{probe}} = 1.7 \times 10^{21}$ cm^{-3}) can therefore traverse the highest densities produced in the experiment of up to 4×10^{19} cm^{-3}. Using time-resolved Faraday rotation polarimetry, we directly capture the magnetic field morphology and evolution in the overdense region (downstream of the critical density) and observe the simultaneous formation of 10-μm-scale, high-amplitude magnetic filaments.

The linearly polarized probe pulse propagates perpendicular to the pump pulse. The probe polarization is sensitive to magnetic fields inside the plasma that are parallel to the probe propagation direction via the Faraday effect. The Faraday rotation angle is given by

$$\varphi_F = \frac{e}{2m_ecn_c^{\text{probe}}}\int_{\mathcal{P}} n_e\vec{B}\cdot d\vec{\ell}, \tag{1}$$

where $\mathcal{P}$ is the path of the probe through the plasma. We measure this polarization rotation using two identical cameras, each equipped with a polarizer biased by $<10^\circ$ on opposite sides of the optimum extinction angle. Details of the reconstruction of polarization angle are outlined in Appendix A.

A wave-front sensor (PHASICS SID4 HR) measures the phase shift of the probe beam due to the plasma. The complex structure of the plasma makes calculating the density from the phase shift less straightforward than for a smooth cylindrically symmetric plasma where Abel inversion is frequently used [32]. We resolve this by treating the bulk plasma and the filaments separately, as outlined in Appendix B.

III. EXPERIMENTAL RESULTS

Figure 2 shows the plasma densities (top) and change in polarization angle (bottom) for three representative shots taken at different delays of the probe relative to the arrival of the LWIR pulse. Shots were taken roughly every 3 ps. Figure 2(a) demonstrates the formation and early expansion of the plasma, with the neutral nitrogen profile of the gas jet shown in green. At this time the first nitrogen electron has been ionized such that the plasma is mostly underdense, and we see a channel in the plasma density that is nearly fully depleted of electrons, likely due to relativistic self-focusing of the laser [33]. At later times [Figs. 2(b) and 2(c)] the channel becomes wider as ions move in response to the radial electric field of the expelled electrons. Assuming the channel expands transversely at the sound speed and that ions are cold, we can estimate the electron temperature to be 70 keV.

The downstream plasma boundary contains filaments of plasma extending into the neutral gas. Surprisingly, as we see in Fig. 2(c), these filaments persist for almost 200 ps without increasing significantly in size, and we do not see clear evidence of filaments merging into larger filaments at later times.

In the polarization angle we see some fine structures of alternating sign, as shown in Figs. 2(d)–2(f). Such structures are indicative of small filaments (assuming a circular cross section) having local azimuthal magnetic fields. The green boxed region shown in Fig. 2(e) was isolated to study the growth of magnetic fields as a function of time, assuming a slab geometry. The characteristic wavelength of the periodic structures in this region is (23.1 ± 3.2) μm. The rms magnetic field strength in this region grows to a maximum of 1 MG at 7.5 ps and falls to 0.3 MG by 193.5 ps as shown in Fig. 2(f). Assuming the magnetic field saturates once hot electrons forming the sheath are trapped within the filaments of wave-number k, $B_{\text{sat}} \approx kv_{\text{hot}}m_ec^2/\pi e$ [3], we can estimate $v_{\text{hot}} \approx 0.70c$ from the peak magnetic field. A similar

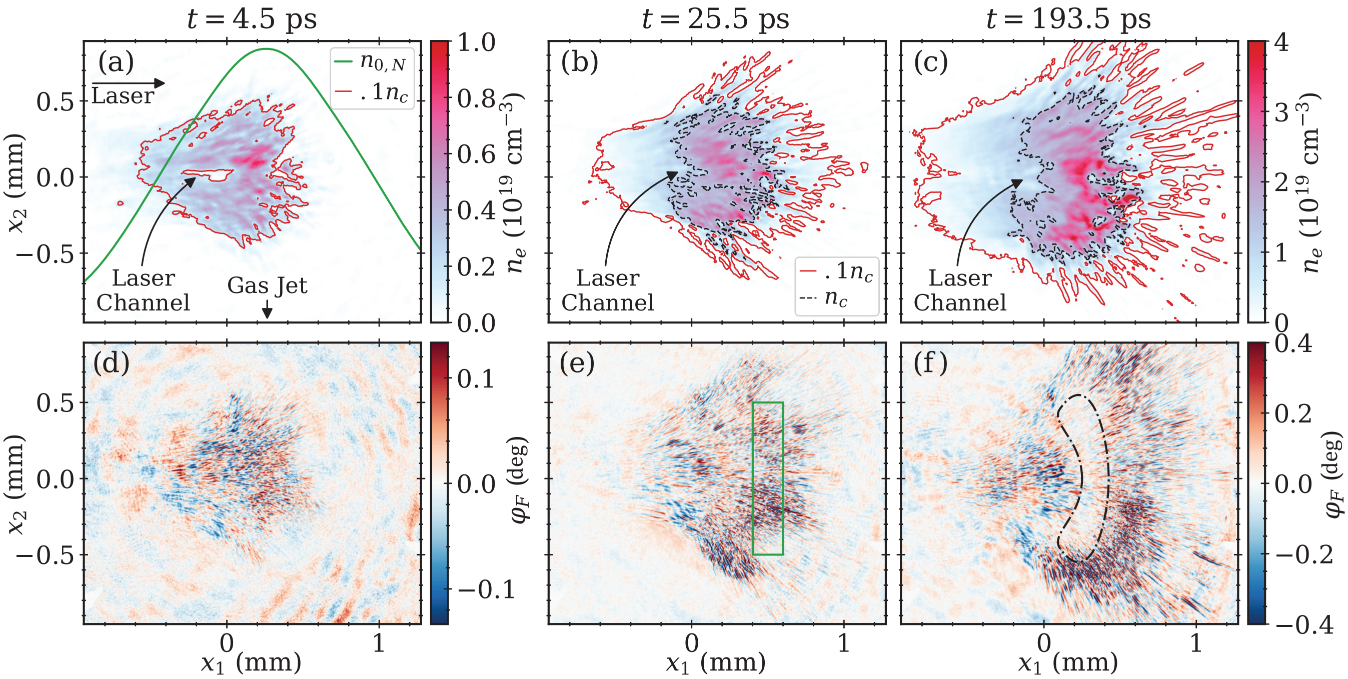

FIG. 2. Plasma density inferred from interferometry (a), (b), and (c) and measured polarization rotation (d), (e), and (f) at various probe delays: (a), (d) 4.5 ps; (b), (e) 25.5 ps; and (c), (f) 193.5 ps in a nitrogen plasma produced by the 2-ps LWIR laser pulse. The neutral nitrogen profile along the laser axis is shown in green in (a). The gas jet is located at $x_2 = -1.5$ mm, outside the field of view. Several density filaments can be seen curving towards the ground plane established by the nozzle in (b) and (c). The red curves in (a), (b), (c) show a contour of the plasma density at 10% of the critical density $n_c = 1.3 \times 10^{19}$ cm^{-3}, while the dashed black curves in (b), (c) show the contour at n_c. The green boxed region in (e) is isolated for Fourier analysis. The black dashed-dotted curve in (f) qualitatively outlines a region of reduced magnetic field.

experimental setup is reported in Ref. [34], but that experiment used a much steeper neutral density ramp, resulting in a shorter laser channel and lower effective hot-electron temperature.

IV. PARTICLE-IN-CELL SIMULATION

We have performed a self-consistent 2D OSIRIS simulation of the interaction of the LWIR laser with an atomic nitrogen gas jet with a peak neutral density below n_c, where multilevel ionization creates an overdense plasma. We used laser parameters consistent with the experiment, and a sloped atomic nitrogen density with a peak of $n_0 = 10^{19}$ cm^{-3} and density gradient scale length of $L_n = 427c/\omega_0 = 0.625$ mm, as shown in green in Fig. 3(a). The laser focus in vacuum is at $x_1 = 0$. Ion motion and collisions were neglected to reduce computational load. Further details of the simulation are outlined in Appendix C.

The laser bores a channel into the plasma [35,36] up to the relativistic critical density $n_{rc} = n_c(1 + a_0^2/2)^{1/2}$ [37], accelerating a population of electrons into the overdense region [38,39]. We note that due to the lack of ion motion here, the laser channel collapses after the laser pulse exits the region.

Space-charge repulsion causes these hot electrons to spread out over a large angle [8], eventually creating an expanding shell of plasma with a much larger volume than the laser spot. A similar expanding cloud of hot electrons was observed to ionize a near-critical-density helium plasma in Ref. [40]. We find that nitrogen atoms are ionized up to the fifth electron within a radius of 100 μm within the region upstream of the laser turning point, giving an on-axis peak plasma density of $n_{rc} = 2.6 \times 10^{19}$ cm^{-3}, at which point the laser can no longer propagate into the plasma.

Figure 3 shows the simulated plasma density (a), longitudinal electric field (b), and out-of-plane magnetic field (c) at $t = 15$ ps. At this time the laser energy has either been dumped into the plasma or reflected at the turning point shown by the black dashed lines. The plasma dynamics are now dominated by hot electrons. The most energetic electrons leave the plasma in the forward direction, setting up an expanding sheath field. Figure 3(b) shows the longitudinal electric field at this time, with the peak field strength of the sheath reaching over 0.3 GV/cm— approaching the estimated threshold field strength for barrier suppression ionization of nitrogen, $E_{\rm BSI} = \pi\epsilon_0 U_{\rm bind}^2/e^3 Z \approx 0.37$ GV/cm, where $U_{\rm bind} = 14.5$ eV is the ionization energy of the outermost electron and $Z = 1$ is the ion charge state after ionization [41]. At the plasma boundary we observe density filaments [Fig. 3(a)] that branch and develop a surrounding azimuthal magnetic field (c). The insets in Fig. 3 show a zoomed-in region around one of these branching filaments, with the 10^{17}-cm^{-3} density contour marked in black. Here, we can see enhancement of the electric field at the filament tips, with the 0.5 $E_{\rm BSI}$ contours shown in green in the inset of Fig. 3(b).

As in streamers [29], this local enhancement of the electric field is caused by space-charge separation as ionized electrons at the filament tip respond to the sheath field faster than the ions. This can be seen directly in simulations including mobile

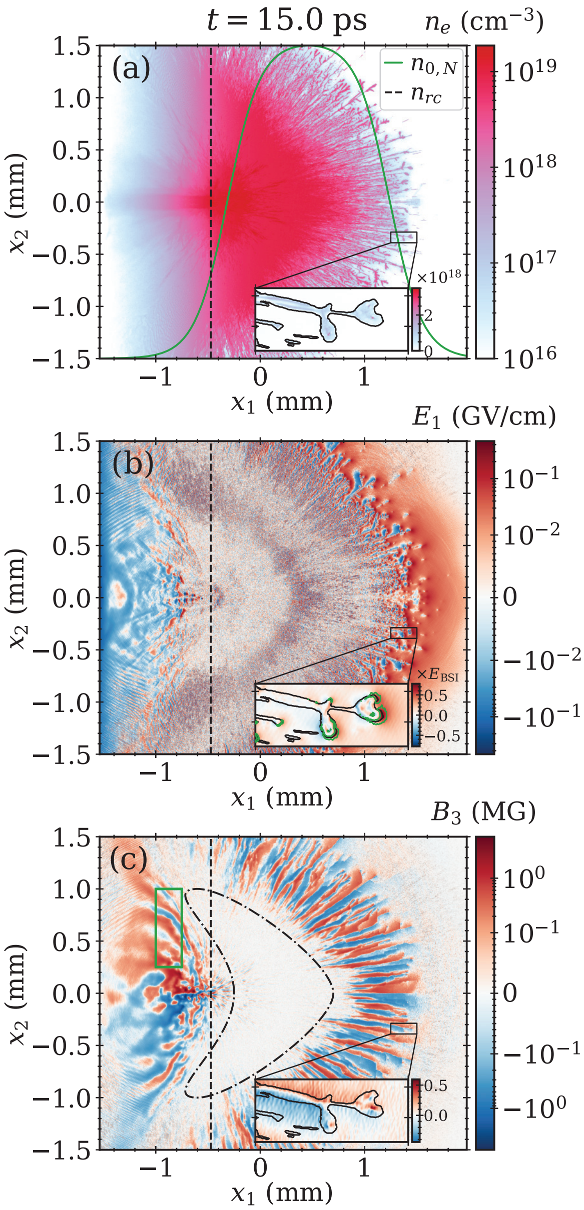

FIG. 3. Simulated (a) plasma density, (b) longitudinal electric field, and (c) out-of-plane magnetic field for nitrogen after 15 ps. The laser enters from left to right. The black dashed lines at $x_1 = -0.5$ mm mark the position of the laser turning point at n_{rc}. The green curve in (a) demonstrates the initial neutral nitrogen profile. The insets show a zoomed view of a single filament on the plasma boundary on linear color scales, with the black contours in (a), (b), and (c) having plasma density of 10^{17} cm^{-3} and the green contours in (b) having $|\vec{E}| = 0.5E_{\rm BSI}$, where BSI stands for barrier suppression ionization. The ionization instability induced by the sheath produces density filaments (a) that act as a current source of the magnetic field filaments shown in (c). The region enclosed by the dashed-dotted black line is filled with uniform-density plasma (a) and almost no filamentary magnetic field (c).

ions, discussed in Appendix D. The enhanced electric field leads to further ionization along that filament, with the ionization front susceptible to branching due to perturbations in the sheath field or plasma density. Modeling of the branching modes in streamer discharge plasmas is an active area of research [42–44]. We note that simulations of a similar laser incident on a preformed plasma show no density or magnetic field filaments in this region as there is no gas to ionize. The average on-axis plasma density and temperature downstream of the laser channel are 6×10^{18} cm^{-3} and 8 keV, respectively. The estimated collisional mean-free path for e-e collisions is 131 mm $\gg L_{x1}$, confirming that our neglect of Coulomb collisions is justified.

Figure 3(c) shows the out-of-plane magnetic field at this time. In the region upstream of n_{rc} (dashed black line) we see Biermann-battery-generated magnetic fields on the leading edge of the plasma ($x_1 \lesssim -1$), partially overlapped by a region of magnetic field filaments without associated density filaments corresponding to the Weibel instability [45]. The green box in Fig. 3(c) contains several of these Weibel filaments. At this time, the mean-temperature anisotropy within the boxed region is 0.6, with the average $T_{\rm hot} \approx 70$ keV and mean magnetic field strength of 0.17 MG. Given the mean density within the box is 3.4×10^{17} cm^{-3}, the fastest-growing Weibel mode for the average plasma conditions inside this box is $k_m \approx 0.37k_p$ [46], corresponding to 160-μm filaments, consistent with the size of the magnetic filaments seen in Fig. 3(c). The interplay of Biermann- and Weibel magnetic fields in overcritical density laser-driven plasmas has been explored in more detail in Ref. [47] as well as more generally in expanding plasmas in Refs. [48,49]. Our findings here are consistent with these results.

A large region past the end of the laser channel is almost free of magnetic field B_3, outlined by the black dashed-dotted lines in Fig. 3(c). This region contains near-uniform plasma that was ionized by the sheath field as the hot electrons expanded ballistically into the neutral gas. As such, this region behaves similarly to preformed plasma, with no persistent magnetic field structures. A similar region can be seen in the experimental data, as outlined in Fig. 2(f). However, deeper into the gas jet on the edge of the plasma the unperturbed sheath field can no longer ionize the gas, and we see magnetic filaments form along the cold-electron density structures as in the inset of Fig. 3(c). The peak field strength within one of these filaments is 0.39 MG, with the dominant $k = 0.41k_p$. Assuming the hot electron $v_{\rm hot} = 0.75c$, and average density of 1.5×10^{18} cm^{-3}, the magnetic field strength at which the hot electrons are trapped within the filament is $B_{\rm sat} \approx k v_{\rm hot} m_e c^2/\pi e = 0.39$ MG [3], matching the peak field strength in the simulation. Thus, the simulated $v_{\rm hot}$ is in reasonable agreement with the experimentally estimated $v_{\rm hot} \approx 0.70c$ from the measured polarization rotation. The absolute scale of the magnetic filaments is larger in simulation than those seen in the experiment. This is due in part to the experimental diagnostic, which is a line-integrated measurement of the product of plasma density and magnetic field, restricting the signal to regions with sufficiently high plasma density. We also anticipate that the 2D simulation cannot fully capture the 3D instability of the ionization front. Because this is a geometric instability, we expect the characteristic wave number to be sensitive to the dimensionality of the system.

The transition from radial sheath expansion due to the ballistic motion of the hot electrons to streamerlike ionization can be seen in the expansion velocity of the plasma. Figure 4 shows the density profile along the laser axis as a function of

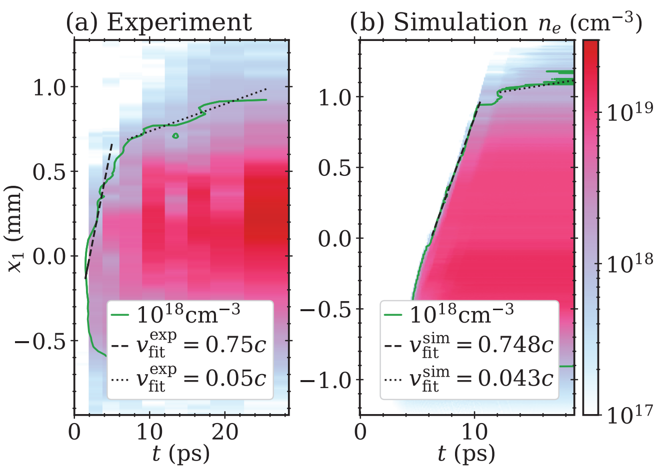

FIG. 4. On-axis density profile as a function of time for (a) experimental data and (b) simulation. The n_e=10^{18}-cm^{-3} contour is shown in green, with two velocities fit at early times (dashed black lines) and late times (dotted black lines).

time for both experimental data (a) and simulation (b). We follow $n_e = 10^{18}$-cm^{-3} contours, shown in green, to determine the expansion velocities at early times where the ballistically expanding hot electrons produce the plasma (dashed black lines) and at later times where the locally enhanced sheath field is ionizing the plasma (dotted black lines). The deduced expansion velocities agree rather well, with $v_{\rm fit}^{\rm exp} = (0.75 \pm 0.01)c$ and $v_{\rm fit}^{\rm sim} = (0.748 \pm 0.002)c$ at early times, consistent with the simulated $v_{\rm hot} = 0.75c$ hot electrons, and $v_{\rm fit}^{\rm exp} = (0.054 \pm 0.001)c$ and $v_{\rm fit}^{\rm sim} = (0.043 \pm 0.003)c$ at later times. However, the transition to streamerlike expansion occurs in the experiment sooner than in the simulations (at 5 vs 10 ps). This is likely a result of the 3D expansion of hot electrons in the experiment, meaning that the hot-electron density decreases more rapidly in the experiment than in the 2D simulation.

V. CONCLUSION

In conclusion, we have developed an experimental platform that allows us to reach densities exceeding the pump laser's critical density while remaining transparent to optical probing of the plasma density and magnetic field structures on the overdense side. Although the Biermann-battery effect and Weibel instability dominate magnetic field generation in the density ramp leading up to the relativistic critical density, the magnetic field dynamics downstream of the critical density region are dominated by locally enhanced ionization occurring in the expanding sheath formed by laser-heated electrons. Supporting simulations show that filamentation and branching of cold plasma occur on a fine scale. These filaments are surrounded by MG azimuthal magnetic fields that persist for over 100 ps. This branching of the ionization front slows down the expansion velocity of the plasma, as seen in both simulation and experiment.

ACKNOWLEDGMENTS

This experiment was carried out at Brookhaven National Laboratory's Accelerator Test Facility. This material is based upon work supported by the U.S. Department of Energy under Grant No. DE-SC0010064, as well as the University of California, Los Angeles and Lawrence Livermore National Laboratory under Grant No. B670378.

DATA AVAILABILITY

The data that support the findings of this article are available from the authors upon reasonable request.

APPENDIX A: RETRIEVAL OF THE FARADAY ROTATION ANGLE

Each of the cameras in the polarimeter has a polarizer in front of it with extinction ratio β_i set to a known angle θ_i, $i = 1, 2$ away from the extinction angle of the probe. The intensity on the camera is

$$I_i(x_1, x_2) = I_0(x_1, x_2)[1 - \beta_i \cos^2 (\varphi_F(x_1, x_2) + \theta_i)].$$

The images from both cameras are first aligned using a spatial fiducial placed at the intermediate image plane shown in Fig. 1. The spatial fiducial consists of four fine-tipped needles, which clearly define four points on each image. We use these points to define a plane-to-plane projection transform from one camera's image plane to the other [50]. This approach allows for subpixel alignment of the two images. Using this differential measurement allows for higher sensitivity to small rotations due to magnetic fields, as signatures of density gradients or plasma self-emission appear in both images and can be removed via subtraction [51,52].

To calibrate the polarimeter we inserted a half wave plate at the interaction point and record measurements at known polarization rotations. When analyzing plasma images, we extract the polarization angle from the ratio of the two images after correcting for the probe intensity profile using images taken with no plasma. For cases where the maximum Faraday rotation angle is expected to be very small, the polarizer angles can be reduced to increase the sensitivity of the diagnostic. Taking the ratio of the two images also removes any structures introduced by density gradients in the plasma or in the probe beam itself, leaving only the signal produced by polarization rotation. For the data shown here the polarizers were set to $\pm 3^\circ$ around extinction.

APPENDIX B: RETRIEVAL OF THE PLASMA DENSITY

The plasma density contains small filaments which do not share the same axis of symmetry as the bulk plasma. This prevents conventional Abel inversion of the probe phase shift recorded by our interferometer. To approximate the density profile we model the plasma density as having two components: a bulk plasma density $n_r(x_1, r \equiv (x_2^2 + x_3^2)^{1/2})$ that is cylindrically symmetric about the laser axis and a slab plasma density $n_s(x_1, x_2)$ that is uniform along the probe line of sight (x_3 axis) for some slab thickness s, such that $n_e(r) \approx n_r(x_1, r) + n_s(x_1, x_2)$.

The phase shift of the probe after passing through the plasma is given by

$$\Delta\varphi(\vec{r}) = \frac{2\pi}{\lambda^{\text{probe}}}\int dx_3\,(\eta(r)-1)$$
$$\approx -\frac{\pi}{\lambda^{\text{probe}}}\int dx_3\,\frac{n_e(r)}{n_c^{\text{probe}}},$$

where $\eta(r)$ is the index of refraction of the plasma, n_c^{probe} is the critical density at the probe wavelength λ^{probe}, and we have taken the approximation $\eta(r) \approx (1 - n_e/n_c^{\text{probe}})^{1/2} \approx 1 - \frac{1}{2}n_e/n_c^{\text{probe}}$ for $n_e \ll n_c^{\text{probe}}$. In this limit we can treat the two components of the density independently such that after exiting the plasma the measured phase shift is

$$\Delta\varphi(x, y) \approx -\frac{\pi}{\lambda^{\text{probe}} n_c^{\text{probe}}}\{\mathcal{A}[n_r(x_1, r)] + n_s(x_1, x_2)s\},$$

where $\mathcal{A}$ is the forward Abel transform. For our data the high-frequency component of the measured phase shift containing the filaments is treated as the uniform slab, while the low frequency is treated as the cylindrically symmetric bulk plasma.

APPENDIX C: DETAILS OF PARTICLE-IN-CELL SIMULATION

The simulation discussed in the text used a domain with $L_{x1} \times L_{x2} = 2400 \times 2400\,(c/\omega_0)^2$ and open boundary conditions for fields and particles. The domain is divided into cells of size $\Delta x = 0.07c/\omega_0$ to resolve both the laser frequency and the higher-plasma frequency in the overdense region, with 16 macroparticles per cell. The initial neutral nitrogen density profile has the form

$$n(x_1) = \tfrac{1}{2}n_0[\tanh{(2(x_1 - x_{10})/L_n)} + 1],$$

where $n_0 = 10^{19}$ cm^{-3} is the peak atomic density, $x_{10} = -0.3$ mm is the position halfway up the ramp, and $L_n = 427c/\omega_0 = 0.625$ mm is the characteristic density gradient scale length. There is an identical density down ramp centered at $x_1 = 1.2$ mm. The simulation includes field ionization via an Ammosov-Delone-Krainov model [25]. We note that in the experiment we use molecular nitrogen, which has a dissociation energy of 9.76 eV [53] before atomic nitrogen is formed and can be ionized sequentially, although other ionization pathways are possible.

The laser parameters match the typical laser parameters in the experiment: $\lambda = 9.2$ μm, linearly polarized in $\hat{x}_3$, $a_0 = 1.85$, $w_0 = 35$ μm, $\tau_{\text{FWHM}} = 2$ ps. While the structures observed in the experiment are certainly 3D, and we expect the filamentation of the ionization front to be of a different characteristic size in the 2D simulation, the scale of the experiment and high plasma densities make 3D simulations computationally infeasible.

APPENDIX D: HYDROGEN SIMULATION WITH MOBILE IONS

The simulation shown in Fig. 3 does not include ion motion, even though over the timescale of our experiment ions are definitely moving. However, simulations including ion motion show the same branching structures on the ionization front, since ion motion is negligible on the timescale of ionization and the formation of the return current. In order to verify that ion motion plays a negligible role in the ionization front instability we are interested in, we performed a second simulation with identical laser parameters and density profile as the nitrogen simulation shown in Fig. 3, instead using hydrogen with a peak neutral density of 5×10^{19} cm^{-3} to match the peak plasma density seen in nitrogen ionized up to the fifth electron. Because there is only one ion species, we were able to simulate ion motion.

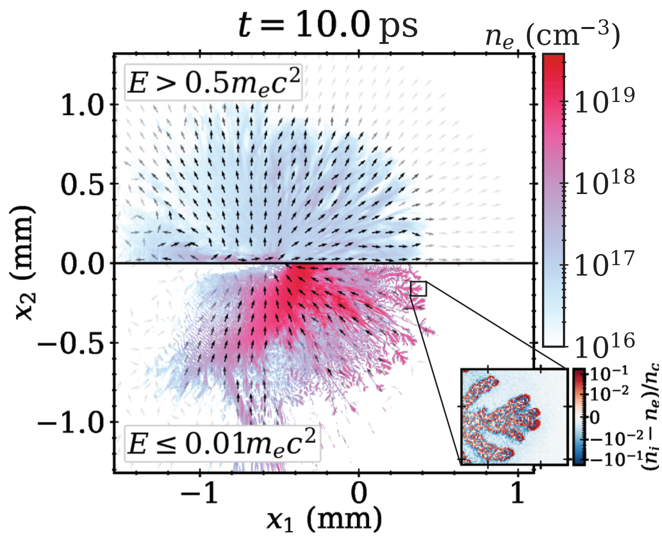

FIG. 5. Simulated hydrogen plasma density for electrons with energies exceeding $0.5m_ec^2$ (top) and $\leqslant 0.01m_ec^2$ (bottom). The black arrows indicate the average direction of electron flow, indicating that the hot-electron population predominantly expands outward while the cold bulk plasma forms the return current. The inset shows a zoomed-in view of the charge density at the tip of a branching filament.

Figure 5 shows the simulated plasma density after 10 ps, where we have separated the plasma into two populations: the laser-heated electrons with energies $>0.5m_ec^2$ (top half) and the bulk plasma with energies $\leqslant 0.01m_ec^2$ (bottom half). As expected, after 10 ps the laser channel is still present due to the motion of hydrogen ions. The black arrows indicate the local direction of electron flow for each population, confirming that the hot electrons are expanding radially outward while the bulk plasma forms the return current. The inset shows the local charge density for a zoomed-in region around one of the branching filament tips, highlighting the surplus of ions right behind the ionization front as the lighter electrons quickly form the return current. We also note that the fine branching structures on the ionization front are only seen in the bulk plasma, while transverse structures of the expanding hot electrons have much longer wavelengths, likely resulting from the conventional beam-plasma instabilities in the overdense region. This differs from the corrugation instability discussed in Refs. [30,31], where the hot-electron filaments drive filamentation of the ionization front.

[1] Y. Sentoku, K. Mima, H. Ruhl, Y. Toyama, R. Kodama, and T. E. Cowan, Laser light and hot electron micro focusing using a conical target, Phys. Plasmas **11**, 3083 (2004).
[2] M. Roth and M. Schollmeier, Ion acceleration—Target normal sheath acceleration, CERN Yellow Reports **1**, 231 (2016).
[3] C. Zhang, C.-K. Huang, and C. Joshi, Self-organization of photoionized plasmas via kinetic instabilities, Rev. Mod. Plasma Phys. **7**, 34 (2023).
[4] N. A. Ebrahim, C. Joshi, D. M. Villeneuve, N. H. Burnett, and M. C. Richardson, Anomalous energy transport to rear surface of microdisks at high laser irradiances, Phys. Rev. Lett. **43**, 1995 (1979).
[5] J. J. Pilgram, C. G. Constantin, H. Zhang, P. Tzeferacos, T. G. Bachmann, L. Rovige, P. V. Heuer, M. B. P. Adams, S. Ghazaryan, M. Kaloyan, R. S. Dorst, M. J.-E. Manuel, and C. Niemann, Two-dimensional Thomson scattering measurements of misaligned electron density and temperature gradients and associated Biermann battery produced fields, Phys. Plasmas **31**, 042113 (2024).
[6] E. S. Weibel, Spontaneously growing transverse waves in a plasma due to an anisotropic velocity distribution, Phys. Rev. Lett. **2**, 83 (1959).
[7] A. Bret, L. Gremillet, and M. E. Dieckmann, Multidimensional electron beam-plasma instabilities in the relativistic regime, Phys. Plasmas **17**, 120501 (2010).
[8] S. Humphries, *Charged Particle Beams* (John Wiley & Sons, Inc., Hoboken, 2013).
[9] M. Tzoufras, C. Ren, F. S. Tsung, J. W. Tonge, W. B. Mori, M. Fiore, R. A. Fonseca, and L. O. Silva, Space-charge effects in the current-filamentation or Weibel instability, Phys. Rev. Lett. **96**, 105002 (2006).
[10] C. Ren, M. Tzoufras, F. S. Tsung, W. B. Mori, S. Amorini, R. A. Fonseca, L. O. Silva, J. C. Adam, and A. Heron, Global simulation for laser-driven MeV electrons in fast ignition, Phys. Rev. Lett. **93**, 185004 (2004).
[11] M. Tatarakis, F. N. Beg, E. L. Clark, A. E. Dangor, R. D. Edwards, R. G. Evans, T. J. Goldsack, K. W. D. Ledingham, P. A. Norreys, M. A. Sinclair, M-S. Wei, M. Zepf, and K. Krushelnick, Propagation instabilities of high-intensity laser-produced electron beams, Phys. Rev. Lett. **90**, 175001 (2003).
[12] M. Manclossi, J. J. Santos, D. Batani, J. Faure, A. Debayle, V. T. Tikhonchuk, and V. Malka, Study of ultraintense laser-produced fast-electron propagation and filamentation in insulator and metal foil targets by optical emission diagnostics, Phys. Rev. Lett. **96**, 125002 (2006).
[13] G. S. Sarkisov, V. V. Ivanov, P. Leblanc, Y. Sentoku, K. Yates, P. Wiewior, O. Chalyy, A. Astanovitskiy, V. Yu. Bychenkov, D. Jobe, and R. B. Spielman, Propagation of a laser-driven relativistic electron beam inside a solid dielectric, Phys. Rev. E **86**, 036412 (2012).
[14] C. Schoenwaelder, A. Marret, S. Assenbaum, C. B. Curry, E. Cunningham, G. Dyer, S. Funk, G. D. Glenn, S. Goede, D. Khaghani, M. Rehwald, U. Schramm, F. Treffert, M. Vescovi, K. Zeil, S. H. Glenzer, F. Fiuza, and M. Gauthier, Time-resolved X-ray imaging of the current filamentation instability in solid-density plasmas, Nat. Commun. **17**, 467 (2026).
[15] C.-K. Huang, C.-J. Zhang, K. A. Marsh, C. E. Clayton, and C. Joshi, Initializing anisotropic electron velocity distribution functions in optical-field ionized plasmas, Plasma Phys. Control. Fusion **62**, 024011 (2020).
[16] C. Zhang, Y. Wu, M. Sinclair, A. Farrell, K. A. Marsh, J. Hua, I. Petrushina, N. Vafaei-Najafabadi, R. Kupfer, K. Kusche, M. Fedurin, I. Pogorelsky, M. Polyanskiy, C.-K. Huang, W. Lu, W. B. Mori, and C. Joshi, Electron Weibel instability induced magnetic fields in optical-field ionized plasmas, Phys. Plasmas **29**, 062102 (2022).
[17] C. Zhang, Y. Wu, M. Sinclair, A. Farrell, K. A. Marsh, I. Petrushina, N. Vafaei-Najafabadi, A. Gaikwad, R. Kupfer, K. Kusche, M. Fedurin, I. Pogorelsky, M. Polyanskiy, C.-K. Huang, J. Hua, W. Lu, W. B. Mori, and C. Joshi, Mapping the self-generated magnetic fields due to thermal Weibel instability, Proc. Natl. Acad. Sci. USA **119**, e2211713119 (2022).
[18] Y. Wu, A. Farrell, M. Sinclair, C. Zhang, I. Petrushina, N. Vafaei-Najafabadi, M. Babzien, W. Li, I. Pogorelsky, M. Polyanskiy, M. Fedurin, K. Kusche, M. Palmer, K. A. Marsh, and C. Joshi, Thermal Weibel instability induced magnetic fields co-exist with linear wakes in laser-ionized plasmas, Phys. Plasmas **31**, 072108 (2024).
[19] B. Allen, V. Yakimenko, M. Babzien, M. Fedurin, K. Kusche, and P. Muggli, Experimental study of current filamentation instability, Phys. Rev. Lett. **109**, 185007 (2012).
[20] S. Mondal, V. Narayanan, W. J. Ding, A. D. Lad, B. Hao, S. Ahmad, W. M. Wang, Z. M. Sheng, S. Sengupta, P. Kaw, A. Das, and G. R. Kumar, Direct observation of turbulent magnetic fields in hot, dense laser produced plasmas, Proc. Natl. Acad. Sci. USA **109**, 8011 (2012).
[21] P. S. M. Claveria *et al.*, Spatiotemporal dynamics of ultrarelativistic beam-plasma instabilities, Phys. Rev. Res. **4**, 023085 (2022).
[22] C. M. Huntington, M. J.-E. Manuel, J. S. Ross, S. C. Wilks, F. Fiuza, H. G. Rinderknecht, H.-S. Park, G. Gregori, D. P. Higginson, J. Park, B. B. Pollock, B. A. Remington, D. D. Ryutov, C. Ruyer, Y. Sakawa, H. Sio, A. Spitkovsky, G. F. Swadling, H. Takabe, and A. B. Zylstra, Magnetic field production via the Weibel instability in interpenetrating plasma flows, Phys. Plasmas **24**, 041410 (2017).
[23] C. M. Huntington, F. Fiuza, J. S. Ross, A. B. Zylstra, R. P. Drake, D. H. Froula, G. Gregori, N. L. Kugland, C. C. Kuranz, M. C. Levy, C. K. Li, J. Meinecke, T. Morita, R. Petrasso, C. Plechaty, B. A. Remington, D. D. Ryutov, Y. Sakawa, A. Spitkovsky, H. Takabe, *et al.*, Observation of magnetic field generation via the Weibel instability in interpenetrating plasma flows, Nat. Phys. **11**, 173 (2015).
[24] P. B. Corkum, Plasma perspective on strong field multiphoton ionization, Phys. Rev. Lett. **71**, 1994 (1993).
[25] N. B. Delone and V. P. Krainov, Tunneling and barrier-suppression ionization of atoms and ions in a laser radiation field, Phys.-Usp. **41**, 469 (1998).
[26] L. V. Keldysh, Ionization in the field of a strong electromagnetic wave, J. Exp. Theor. Phys. **20**, 56 (1964).
[27] N. H. Burnett and P. B. Corkum, Cold-plasma production for recombination extreme-ultraviolet lasers by optical-field-induced ionization, J. Opt. Soc. Am. B **6**, 1195 (1989).
[28] M. Arrayás, S. Betelú, M. A. Fontelos, and J. L. Trueba, Fingering from ionization fronts in plasmas, SIAM J. Appl. Math. **68**, 1122 (2008).
[29] S. Nijdam, J. Teunissen, and U. Ebert, The physics of streamer discharge phenomena, Plasma Sources Sci. Technol. **29**, 103001 (2020).

[30] S. I. Krasheninnikov, A. V. Kim, B. K. Frolov, and R. Stephens, Intense electron beam propagation through insulators: Ionization front structure and stability, Phys. Plasmas **12**, 073105 (2005).

[31] A. Debayle and V. T. Tikhonchuk, Filamentation instability of a fast electron beam in a dielectric target, Phys. Rev. E **78**, 066404 (2008).

[32] D. W. Oldenburg and J. C. Samson, Inversion of interferometric data from cylindrically symmetric, refractionless plasmas, J. Opt. Soc. Am. **69**, 927 (1979).

[33] C. E. Max, J. Arons, and A. B. Langdon, Self-modulation and self-focusing of electromagnetic waves in plasmas, Phys. Rev. Lett. **33**, 209 (1974).

[34] N. P. Dover, O. Tresca, N. Cook, O. C. Ettlinger, R. J. Kingham, C. Maharjan, M. N. Polyanskiy, P. Shkolnikov, I. Pogorelsky, and Z. Najmudin, Optical imaging of laser-driven fast electron Weibel-like filamentation in overcritical density plasma, Phys. Rev. Lett. **134**, 025102 (2025).

[35] C. Gong, S. Y. Tochitsky, F. Fiuza, J. J. Pigeon, and C. Joshi, Plasma dynamics near critical density inferred from direct measurements of laser hole boring, Phys. Rev. E **93**, 061202(R) (2016).

[36] A. Pukhov and J. Meyer-ter-Vehn, Laser hole boring into overdense plasma and relativistic electron currents for fast ignition of ICF targets, Phys. Rev. Lett. **79**, 2686 (1997).

[37] L. Ji, B. Shen, and X. Zhang, Transparency of near-critical density plasmas under extreme laser intensities, New J. Phys. **20**, 053043 (2018).

[38] A. Pukhov, Z.-M. Sheng, and J. Meyer-ter-Vehn, Particle acceleration in relativistic laser channels, Phys. Plasmas **6**, 2847 (1999).

[39] S. C. Wilks, Simulations of ultraintense laser–plasma interactions, Phys. Fluids B **5**, 2603 (1993).

[40] F. Sylla, A. Flacco, S. Kahaly, M. Veltcheva, A. Lifschitz, V. Malka, E. d'Humières, I. Andriyash, and V. Tikhonchuk, Short intense laser pulse collapse in near-critical plasma, Phys. Rev. Lett. **110**, 085001 (2013).

[41] S. Augst, D. Strickland, D. D. Meyerhofer, S. L. Chin, and J. H. Eberly, Tunneling ionization of noble gases in a high-intensity laser field, Phys. Rev. Lett. **63**, 2212 (1989).

[42] M. Arrayás, M. A. Fontelos, and C. Jiménez, Contour dynamics model for electric discharges, Phys. Rev. E **81**, 035401(R) (2010).

[43] D. Wang, L. Wang, and Y. Zheng, Particle-in-cell/Monte Carlo collisional simulation of negative streamer formation and branching between planar electrodes, J. Appl. Phys. **124**, 203301 (2018).

[44] Z. Zhao, R. J. Dijoud, and Y. Fu, A tutorial demonstration of streamer physics via fluid simulations, Phys. Plasmas **32**, 110901 (2025).

[45] A. Farrell, M. Sinclair, Y. Wu, K. Marsh, A. Gaikwad, N. Vafaei-Najafabadi, M. Babzien, W. Li, M. Polyanskiy, I. Pogorelsky, C. Zhang, and C. Joshi, Biermann battery effect, Weibel instability, and ionization-driven filamentation in picosecond, relativistic laser-produced gas jet plasmas (unpublished).

[46] R. C. Davidson, Kinetic waves and instabilities in a uniform plasma, *Basic Plasma Physics* (North-Holland Publishing, 1983), Vol. 1, pp. 519–585.

[47] N. Shukla, K. Schoeffler, E. Boella, J. Vieira, R. Fonseca, and L. O. Silva, Interplay between the Weibel instability and the Biermann battery in realistic laser-solid interactions, Phys. Rev. Res. **2**, 023129 (2020).

[48] K. M. Schoeffler, N. F. Loureiro, R. A. Fonseca, and L. O. Silva, Magnetic-field generation and amplification in an expanding plasma, Phys. Rev. Lett. **112**, 175001 (2014).

[49] K. M. Schoeffler, N. F. Loureiro, R. A. Fonseca, and L. O. Silva, The generation of magnetic fields by the Biermann battery and the interplay with the Weibel instability, Phys. Plasmas **23**, 056304 (2016).

[50] A. Criminisi, I. Reid, and A. Zisserman, A plane measuring device, Image Vis. Comput. **17**, 625 (1999).

[51] Y.-Y. Chang, X. Cheng, A. Hannasch, M. LaBerge, J. M. Shaw, K. Weichman, J. Welch, A. C. Bernstein, W. Henderson, R. Zgadzaj, and M. C. Downer, Faraday rotation study of plasma bubbles in GeV wakefield accelerators, Phys. Plasmas **28**, 123105 (2021).

[52] M. C. Kaluza, H.-P. Schlenvoigt, S. P. D. Mangles, A. G. R. Thomas, A. E. Dangor, H. Schwoerer, W. B. Mori, Z. Najmudin, and K. M. Krushelnick, Measurement of magnetic-field structures in a laser-wakefield accelerator, Phys. Rev. Lett. **105**, 115002 (2010).

[53] P. Wang, S. Gong, Y. Li, and Y. Mo, Bond dissociation energy of N_2 measured by state-to-state resolved threshold fragment yield spectra, J. Chem. Phys. **160**, 014304 (2024).